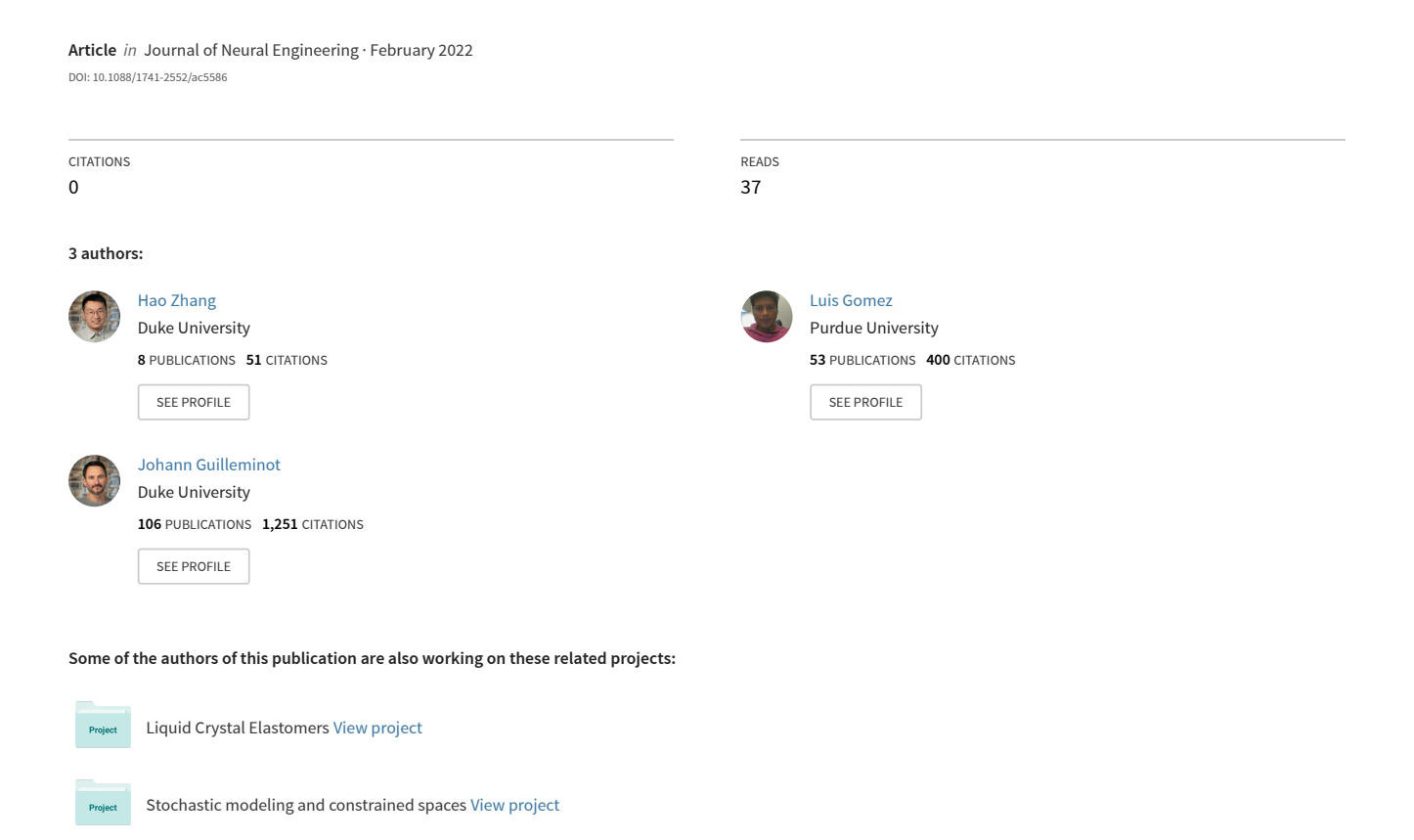
Uncertainty quantification of TMS simulations considering MRI segmentation errors



PAPER

Uncertainty quantification of TMS simulations considering MRI segmentation errors

To cite this article: Hao Zhang et al 2022 J. Neural Eng. 19 026022

View the article online for updates and enhancements.

You may also like

- Electric field measurement of two commercial active/sham coils for transcranial magnetic stimulation J Evan Smith and Angel V Peterchev
 - D Evan Smith and Angel v Peterchev
- <u>Coil model comparison for cerebellar transcranial magnetic stimulation</u>
 M Kaan Çan, Ilkka Laakso, Jaakko O Nieminen et al.
- An optical setup for electric field measurements in MRI with high spatial resolution

Simon Reiss, Andreas Bitzer and Michael Bock

Journal of Neural Engineering



RECEIVED 11 August 2021

REVISED
10 January 2022

ACCEPTED FOR PUBLICATION

ACCEPTED FOR PUBLICATION 8 February 2022

PUBLISHED 30 March 2022

PAPER

Uncertainty quantification of TMS simulations considering MRI segmentation errors

Hao Zhang¹, Luis J Gomez^{2,*} o and Johann Guilleminot¹

- ¹ Department of Civil and Environmental Engineering, Duke University, Durham, NC, 27710, United States of America
- Department of Electrical and Computer Engineering, Purdue University, West Lafayette, IN, 47907, United States of America
- * Author to whom any correspondence should be addressed.

E-mail: ljgomez@purdue.edu

Keywords: TMS simulation, non-Gaussian random field, uncertainty quantification, patient-specific brain geometry Supplementary material for this article is available online

Abstract

Objective. Transcranial magnetic stimulation (TMS) is a non-invasive brain stimulation method that is used to study brain function and conduct neuropsychiatric therapy. Computational methods that are commonly used for electric field (E-field) dosimetry of TMS are limited in accuracy and precision because of possible geometric errors introduced in the generation of head models by segmenting medical images into tissue types. This paper studies E-field prediction fidelity as a function of segmentation accuracy. Approach. The errors in the segmentation of medical images into tissue types are modeled as geometric uncertainty in the shape of the boundary between tissue types. For each tissue boundary realization, we then use an in-house boundary element method to perform a forward propagation analysis and quantify the impact of tissue boundary uncertainties on the induced cortical E-field. Main results. Our results indicate that predictions of E-field induced in the brain are negligibly sensitive to segmentation errors in scalp, skull and white matter (WM), compartments. In contrast, E-field predictions are highly sensitive to possible cerebrospinal fluid (CSF) segmentation errors. Specifically, the segmentation errors on the CSF and gray matter interface lead to higher E-field uncertainties in the gyral crowns, and the segmentation errors on CSF and WM interface lead to higher uncertainties in the sulci. Furthermore, the uncertainty of the average cortical E-fields over a region exhibits lower uncertainty relative to point-wise estimates. Significance. The accuracy of current cortical E-field simulations is limited by the accuracy of CSF segmentation accuracy. Other quantities of interest like the average of the E-field over a cortical region could provide a dose quantity that is robust to possible segmentation errors.

1. Introduction

Transcranial magnetic stimulation (TMS) is a non-invasive brain stimulation technique that is widely used in the neurosciences for studying brain function [1–5] and to treat psychiatric and neurological disorders [6–9]. During TMS a coil driven by brief current pulse induces an electric field (E-field) in the brain. The E-field is considered the 'active ingredient' of TMS that elicits and modulates brain activity [10]. As a result, E-field dosimetry is critical for the development of novel TMS protocols. For E-field dosimetry computational simulations are becoming commonplace because there are no established methods for non-invasively measuring the cortical

E-fields [7] induced during TMS. Correspondingly, there is a need to develop a quantitative characterization of the accuracy of TMS simulations. Recent studies have quantified numerical accuracy [11, 12], sensitivity to conductivity uncertainty [13, 14], and coil placement errors [15, 16] of TMS simulations. This paper quantifies the magnitude of the error in the TMS simulation predicted E-field induced in the brain as a function of patient head model uncertainty.

Computational simulations for predicting the TMS induced E-fields require a model of the subject's head, the TMS coil and their relative placement. Modeling errors in the predicted E-field can result from limited accuracy of the head model, which is typically derived from MRI images that are

segmented into individual tissue compartments [13, 17, 18]. For example, Dice coefficient, a measurement of relative overlap between two segmentations, has been used to compare automatic segmented gray and white matter (GM and WM) outputs to manually segmented images. All of these tests consistently have indicated Dice scores around 0.9 [19, 20]. Furthermore, gray matter thickness differed from -0.79to 0.65 mm (90% confidence interval)[21] between automatic segmentation predictions and postmortem gray matter thickness measurements. Finally, average Hausdorff distance, another measure of similarity between two shapes, has been used to estimate segmentation errors. Typically observed average Hausdorff distance errors are in the order of magnitude of 0.1 mm [19, 20]. All of these results indicate that existing automatic MRI image segmentation pipelines achieve excellent precision at segmenting brain tissues; however, they are not perfect. Furthermore, non-brain tissues have larger errors associated with them [22, 23]. Apart from errors, soft tissue boundaries do not have fixed shapes. They can move depending on posture. For example, cerebrospinal fluid (CSF) tissue boundary shape can vary based on the position of the subject [24]. Aside from head model shape errors there is also tissue conductivity uncertainty. However, these have been shown to result in negligible error relative to other sources of uncertainty and are not considered here [13, 14].

There is evidence indicating that the E-field is sensitive to head model uncertainty. For example, it was found that sulci E-fields are highly dependent to sulci width [25]. Different segmentation pipelines, which result in distinct head models for the same imaging data, generate significantly different E-field predictions [20, 22]. Furthermore, the effects of bias in segmentation algorithms were studied by systematically biasing a one-vs-all tissue segmentation classifier to preferentially predict a given tissue type [26]. Results showed that there is a strong dependence on CSF, GM, and WM shape to TMS predicted E-field. However, to date a systematic parametric study of the dependence of head model tissue shape uncertainty to E-field prediction uncertainty has not been done.

Random fields [27] are commonly used to model parameter or shape uncertainties for a number of applications including global temperature distribution [28], material parameter modeling [29, 30], additive manufacturing of biomaterials [31], and brain surfaces [32]. Recently, we proposed an approach involving a stochastic partial differential equation (SPDE) to model segmented tissue boundary shape uncertainty and geometrical defects in 3D printed structures [33]. Here, possible tissue segmentation errors are modeled as a tissue shape uncertainty, and realizations of the perturbed tissue shape are constructed by sampling a random field on the tissue surface. This random field defines the magnitude

of a perturbation along the normal direction to the nominal surface. Hence, each tissue shape realization slightly differs from the segmentation output nominal tissue boundaries and allows us to model possible segmentation errors as a tissue boundary shape uncertainty. The goals of this paper are to quantify the extent that tissue boundary shape uncertainty limits the fidelity of E-field predictions, and to identify the key tissue boundaries that contribute most to cortical E-field prediction uncertainty. These results will enable the determination of key E-field related quantities that are robust to segmentation errors. For example, we observe that averaging E-fields over a small region provides E-field predictions that are more robust to segmentation errors.

The rest of the paper is organized as follows. In the methods section we describe our shape uncertainty distribution and how to generate samples of it. Then, we provide details of our boundary element method (BEM) solver and head models used in this study. In the results sections we provide validation examples validating the accuracy of our SPDE method for generating Gaussian correlated samples relative to other methods, and we study the effects of tissue boundary uncertainty on predicted cortical E-field. The conclusions and discussion sections summarize key findings of our study.

2. Material and methods

2.1. Overview

Computational frameworks for TMS E-field dosimetry [9, 23] typically use segmentation toolboxes to generate head models from structural MRI images. Commonly used head segmentation toolboxes for generating head models from MRI images include volume based ones (e.g. SPM [34], CondNet [35]) and surface based ones (e.g. freesurfer [36], and fastsurfer [19]). The volume based ones employ a onevs-all strategy to classify each MRI image voxel into a tissue type [26, 34]. Surface based segmentation toolboxes determine the boundary between different tissue types [36]. Independent of segmentation method, the output is then converted to surface boundary triangle or volume tetrahedron mesh models of the subject head for use in BEM or FEM simulation, respectively. All of these head models will have limited accuracy because of potential errors in the segmentation process resulting from low image contrast between tissue types, movement artifacts, partial volume effects, noise, and others.

Due to all of these potential errors, the head model output of the segmentation toolboxes has some uncertainty associated with it. In this paper, we treat each boundary surface of the head model output of the segmentation as a nominal surface Γ , and uncertainty is modeled as a random perturbation to Γ , denoted by $\widetilde{\Gamma}$ (figure 1); see [33]. The coordinates

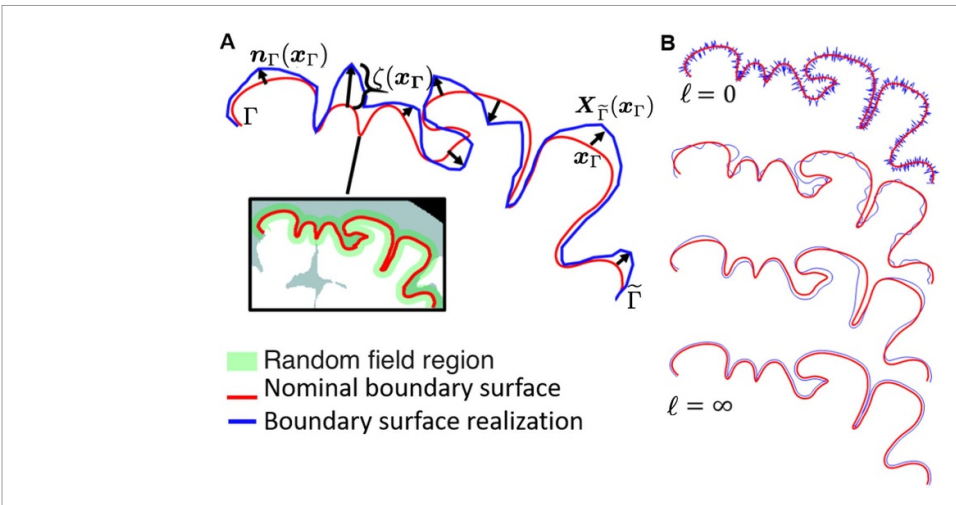


Figure 1. Sketches on how the geometric uncertainties are generated on brain tissue boundaries. (A) Realizations of the boundary surface $\widetilde{\Gamma}$ are generated via displacing each node location \mathbf{x}_{Γ} on the nominal boundary surface Γ by an amount $\zeta(\mathbf{x}_{\Gamma})$ along the normal direction $\mathbf{n}_{\Gamma}(\mathbf{x}_{\Gamma})$. The green band denotes the perturbation region with \pm standard deviation. (B) The correlation length ℓ of the random field $\zeta(\mathbf{x}_{\Gamma})$ controls the level of smoothness of each realization. The perturbations would be totally uncorrelated within each node when $\ell=0$, while the perturbations become totally homogeneous when $\ell=\infty$. The smoothness of realizations increases with increasing ℓ .

of the points defining the perturbed surface $\widetilde{\Gamma}$ are defined as

$$X_{\widetilde{\Gamma}}(x_{\Gamma}) = x_{\Gamma} + \zeta(x_{\Gamma})n_{\Gamma}(x_{\Gamma}), \quad \forall x_{\Gamma} \in \Gamma,$$
 (1)

where $n_{\Gamma}(x_{\Gamma})$ is an outward unit normal vector and $\{\zeta(\mathbf{x}_{\Gamma}), \mathbf{x}_{\Gamma} \in \Gamma\}$ is a non-Gaussian random field indexed by Γ . In practice, and following the equation above, a realization Γ of the perturbed tissue surface is obtained by displacing each location x_{Γ} of the original nominal surface Γ by an amount $\zeta(\mathbf{x}_{\Gamma})$ along the normal direction $n_{\Gamma}(x_{\Gamma})$. Hence, the central task for perturbation generation is the definition of the non-Gaussian field $\{\zeta(\mathbf{x}_{\Gamma}), \mathbf{x}_{\Gamma} \in \Gamma\}$. To accomplish this, a Gaussian field with a Matérn-type covariance function is first generated, and a transport map T is subsequently used to map the latent Gaussian field to a non-Gaussian field exhibiting bounded variations. In our setting, the Matérn covariance function is parameterized in terms of a geodesic distance in order to capture the curvature and complex folds exhibited by brain tissue surfaces.

Each step of the segmentation error uncertainty quantification process (figure 2) is explained in the next few sections. First, the head model is generated using an automatic segmentation and meshing framework (figure 2(A)). Here we used the Ernie head model [22]. Then, an ensemble of head models is generated using the SPDE approach and the head model tissue boundary meshes (figure 2(B)). To fix the self-intersecting meshes after modifying the boundary meshes, a conditional sampling method is employed as described in [33]. For each head model, an E-field simulation is run (figure 2(C)). Finally, ensemble E-field statistics are estimated. The last methods section describes the methods used for choosing shape uncertainty parameters (or

perturbation parameters) that result in uncertainty that is representative of automatic segmented head model uncertainty.

2.2. Discretization of shape uncertainty

This section briefly summarizes the main results in [33] with an emphasis on defining the perturbation parameters. We refer interested readers to [33] for implementation details and further technical derivations. Below, we start by introducing the SPDE method, which is used to construct a latent Gaussian random field $\{\Xi(\mathbf{x}_{\Gamma}), \mathbf{x}_{\Gamma} \in \Gamma\}$ with a Matérn covariance structure. We then present the construction of a transport map T that pushes forward the Gaussian random field to a non-Gaussian random field exhibiting a Beta first-order marginal distribution (that is, $\zeta(\mathbf{x}_{\Gamma}) = T(\Xi(\mathbf{x}_{\Gamma}))$).

The latent field is chosen as a centered Gaussian random field with a Matérn covariance function given, in \mathbb{S}^2 , by

$$C(\mathbf{x}, \mathbf{y}) = \sigma^2 \frac{2^{1-\nu}}{\mathbb{G}(\nu)} \left(\frac{\|\mathbf{x} - \mathbf{y}\|}{\ell} \right)^{\nu} K_{\nu} \left(\frac{\|\mathbf{x} - \mathbf{y}\|}{\ell} \right),$$
$$\forall \mathbf{x}, \mathbf{y} \in \mathbb{S}^2, \tag{2}$$

where \mathbb{S}^2 denotes the two-dimensional manifold embedded \mathbb{R}^3 , $\|\cdot\|$ is the geometric distance defined on two-dimensional manifold, σ^2 is the marginal variance of the field, \mathbb{G} is the Gamma function, $\ell>0$ and $\nu>0$ are the correlation length and smoothness perturbation parameters, and K_{ν} is the modified Bessel function of the second kind (of order ν). The parameter ν controls, in particular, the meansquare differentiability of the field. For $\nu=1/2$ and $\nu\to+\infty$, the Matérn covariance function reduces to the standard exponential and squared exponential covariance functions, respectively. In this study, we

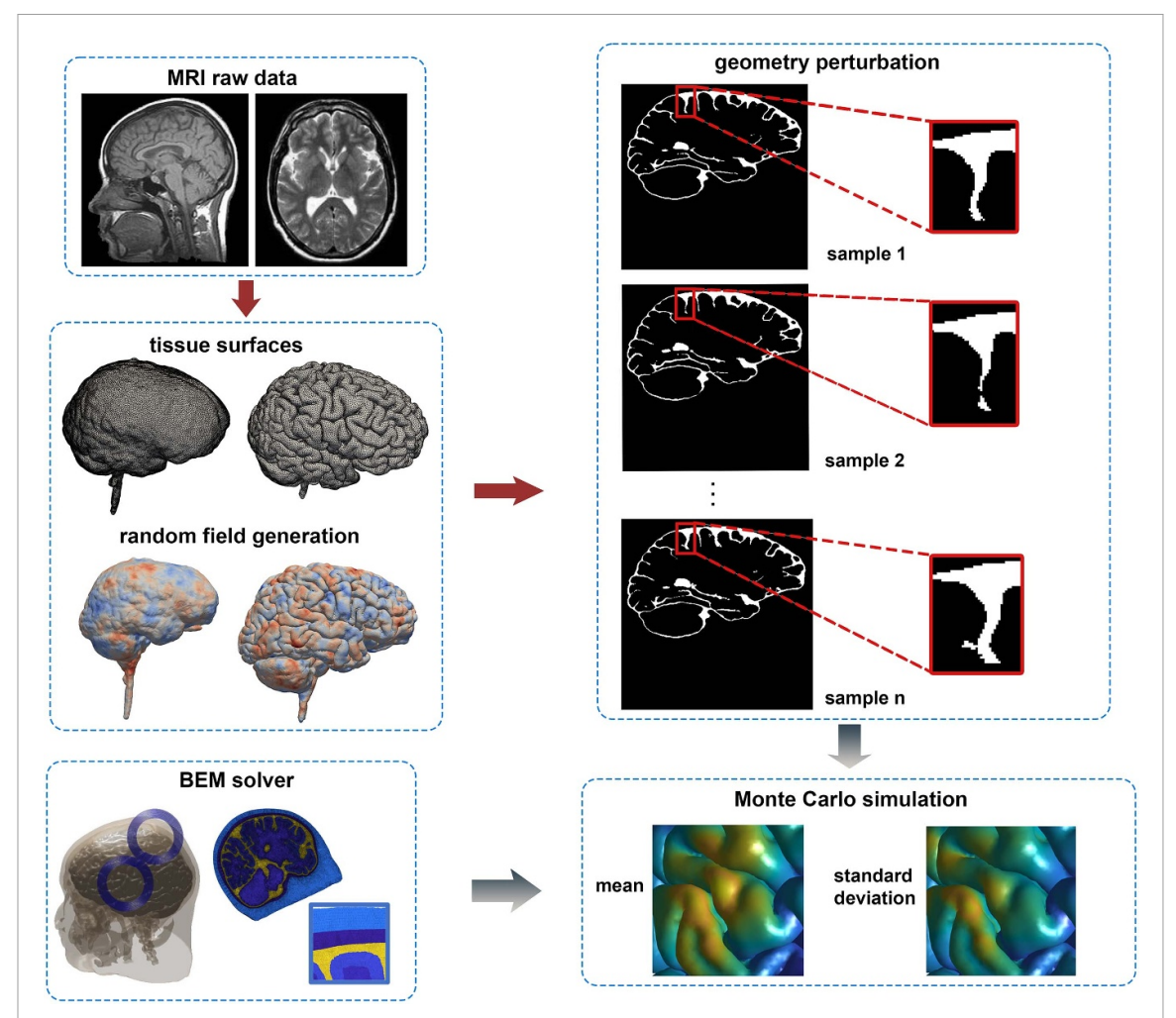


Figure 2. The overall workflow. Firstly, some regular segmentation tools are employed to segment the MRI raw data and further generate the brain tissue surfaces, which are used as the nominal surfaces. Then the non-Gaussian random field is defined and sampled on the tissue boundaries, and the geometric perturbations can be generated accordingly. Finally, the BEM solver is employed to solve the E-field by running Monte Carlo simulations.

choose $\nu=1$. The correlation length parameter ℓ controls the rate of decay of the correlation function and mediates the curvature of the realizations for the perturbed surface $\widetilde{\Gamma}$. Large correlation lengths result in slow decays and hence, yield to perturbed surfaces that mostly have low curvatures. In contrast, small correlation lengths lead to perturbed surfaces with larger curvatures, owing to the fast decay of the correlation function. This effect can clearly be observed in figure 1, where cross sections of the nominal surface (red curve), along with cross sections of realizations of the random field (blue curve), are shown for different values of ℓ . It is seen, in particular, that the realization becomes smoother as the correlation parameter ℓ is increased.

Following the work by Whittle [37], the Gaussian field is defined and sampled through the SPDE

$$(\kappa^2 \mathcal{I} - \Delta)^{\alpha/2} \Xi = \dot{W},\tag{3}$$

where $\kappa = 1/\ell$, ℓ denotes the correlation length parameter, \mathcal{I} and Δ are the identity and Laplacian operators, $\alpha = (\nu + d/2)$, \dot{W} denotes the normalized

Gaussian white noise in \mathbb{R}^d , and equality holds in the sense of distributions. The conditional variance of the random field is given as

$$\sigma^2 = \frac{\mathbb{G}(\nu)}{\mathbb{G}(\nu + d/2)(4\pi)^{d/2}\kappa^{2\nu}}.$$
 (4)

Here, the SPDE is defined and solved on the manifold corresponding to the nominal surface Γ , using the Galerkin approach proposed in [28]. This strategy allows us to capture the geometric complexity of the brain surfaces on the fly, so that shape uncertainties can be generated in a consistent way. The description of that component is fairly technical, and we refer readers to [33] and the references therein for details.

Once the latent Gaussian field $\{\Xi(\mathbf{x}_{\Gamma}), \mathbf{x}_{\Gamma} \in \Gamma\}$ has been defined, the next step is to introduce a transformation T such that the geometric perturbations are bounded almost surely. Here we consider a symmetric support $[-\varepsilon, \varepsilon]$ for these perturbations, where ε is the maximum magnitude of the (positive or negative) perturbation at a given location. In order to construct an objective probabilistic model

under such a boundedness constraint, the maximum entropy principle is invoked. Considering repulsion constraints at the boundary of the support, it can be shown that T must be chosen such that the pushed forward variable (at any fixed location) exhibits a Beta distribution [33]. We therefore define T through the relationship

$$\zeta(\mathbf{x}_{\Gamma}) = 2 \varepsilon F_{\mathcal{B}(\alpha,\alpha)}^{-1} \left(F_{\mathcal{N}(0,1)} (\Xi(\mathbf{x}_{\Gamma})) \right) - \varepsilon,$$

$$\forall \mathbf{x}_{\Gamma} \in \Gamma, \tag{5}$$

where $F_{\mathcal{B}(\alpha,\beta)}^{-1}$ is the inverse cumulative distribution function of the Beta law with hyperparameters α and β (here, we set $\alpha=\beta$ to obtain a symmetric distribution), and $F_{\mathcal{N}(0,1)}$ is the cumulative distribution function of the normalized Gaussian distribution. It follows that the random field is centered, i.e.

$$\mathbb{E}\{\zeta(\mathbf{x}_{\Gamma})\}=0$$

with \mathbb{E} the operator of mathematical expectation, and the variance is obtained as

$$\sigma^2\{\zeta(\mathbf{x}_{\Gamma})\} = \frac{\varepsilon^2}{1+2\alpha}.$$
 (6)

From a computational standpoint, notice that we use conditional sampling to ensure that the random field does not contain self-intersecting meshes, as explained in [33].

2.3. Boundary element solver

The TMS driving coil currents are J(x, t) = P(t)J(x), where P(t) is the current pulse-waveform, J(x) is the spatial variation of the current, t is time, and xis a Cartesian coordinate. These currents generate a total E-field $\mathbf{E}_{tot}(\mathbf{x},t) = P'(t)\mathbf{E}_{tot}(\mathbf{x})$, where P'(t) is the time-derivative of the pulse-waveform, and $E_{tot}(x)$ is the spatial variation of the E-field. Since the E-field is trivially dependent on P(t), the BEM is used to solve for $E_{tot}(x)$ using J(x) and the results are re-scaled to obtain $E_{tot}(\mathbf{x},t)$. First, the total E-field $E_{tot}(\mathbf{x})$ is decomposed into a primary E-field $E_{D}(x)$, where xis a Cartesian coordinate), that is the E-field generated by the coil in the absence of the head, and the secondary E-field $E_s(x)$ that is induced by accumulated charges $\rho(x)$ on the brain tissue interfaces. The primary E-field E_p is

$$E_p(\mathbf{x}) = -\frac{\mu_0}{4\pi} \int \frac{J(\mathbf{x'})}{\|\mathbf{x} - \mathbf{x'}\|} d\mathbf{x'}, \tag{7}$$

where μ_0 is the permeability of the free space. The secondary E-field is the following

$$E_s(\mathbf{x}) = -\nabla \frac{1}{4\pi\epsilon_0} \int \frac{\rho(\mathbf{x'})}{\|\mathbf{x} - \mathbf{x'}\|} d\mathbf{x'}, \quad (8)$$

where ε_0 is the permittivity of free-space and $\rho(\mathbf{x})$ is an unknown charge density residing on tissue

boundaries. At each interface, the charge density is determined by applying the electromagnetic boundary condition

$$\langle \boldsymbol{n}, \sigma^+ \boldsymbol{E}_{\text{tot}}^+ \rangle = \langle \boldsymbol{n}, \sigma^- \boldsymbol{E}_{\text{tot}}^- \rangle,$$
 (9)

where n is the outward unit vector normal to the boundary, $\langle n, E_{\rm tot}^+ \rangle$ and $\langle n, E_{\rm tot}^- \rangle$ are the total E-field along the normal direction an infinitesimal away from the tissue boundary into the outer and inner head tissue compartment, respectively, and σ^- and σ^+ are the conductivities of the inner and outer head tissue compartments, respectively. The above boundary condition results in the following integral equation defined on each tissue boundary

$$\frac{1}{2}\rho(\mathbf{x}) + \frac{\sigma^{+} - \sigma^{-}}{\sigma^{+} + \sigma^{-}}$$

$$< \frac{1}{4\pi} \int_{p.v.} \rho(\mathbf{x'}) \frac{\mathbf{x} - \mathbf{x'}}{||\mathbf{x} - \mathbf{x'}||^{3}} d\mathbf{x'}, \mathbf{n}(\mathbf{x}) >$$

$$= -\frac{\sigma^{+} - \sigma^{-}}{\sigma^{+} + \sigma^{-}} \epsilon_{0} < E_{p}(\mathbf{x}), \mathbf{n}(\mathbf{x}) >, \qquad (10)$$

where 'p.v.' is used to denote Cauchy principal value. The BEM described in [38] is used to solve equation (10) for the charge distribution $\rho(x)$ on the interface. In equation (10), the charge distribution is defined on tissue interfaces and as a result, the TMS simulation can be conducted only using the boundary mesh of brain tissue interfaces, without generating volume mesh in the brain, which reduces the computation cost. The BEM solver used here is freely-available online (see [39]), and implementation details are can be found in [38].

2.4. Shape uncertainty calibration metrics

The segmentation tools assign each voxel of structural MRI image into one of five tissue types either scalp, skull, CSF, grey matter (GM) or WM. These segmentations are then used to extract boundaries between different tissues types. Each tissue surface is indicated by its two adjacent tissues (i.e. air/scalp, scalp/skull, skull/CSF, CSF/GM and GM/WM) as depicted in figure 3(A). There have been various metrics that have been used to measure segmentation accuracy. Here we use the Dice score (*DICE*), one of the most used metrics, defined as

$$DICE(A,B) = \frac{2 \times A \cap B}{A+B},\tag{11}$$

where *A*, *B* correspond to the two separate index sets, each set composed with Boolean values, 1 denoting the node inside the domain, and 0 denoting the node outside the domain. The Dice score is calculated for each tissue compartment separately. To calculate the Dice score for a tissue compartment we count the number of voxels in the unperturbed and perturbed compartment region separately, denoted as *A* and

B in the above equation. Then the Dice coefficient can be calculated as $DICE = (2 \times N_{overlap})/(N_{pert} +$ N_{unpert}), where $N_{overlap}$ denotes the number of overlapping voxels in the two vertices sets, N_{pert} and N_{unpert} denotes the number of voxels in the perturbed and unperturbed gray matter region. The closer the Dice score is to 1, the less variations the tissue volume has, and vice versa. To determine the approximate perturbation ranges on the surfaces, we calculate the Dice scores of each tissue given several different perturbation parameters, and make the Dice scores comparable with the reference results in [20] for each tissue type, i.e. the skin, skull, CSF, GM and WM. There are two major random field parameters employed in this work to control the variation of tissue shapes, i.e. the perturbation heights ε and correlation length ℓ . To make the random fields comparable, the variance shown in equation (6) is selected such that the coefficient of variation of the non-Gaussian random field $(CV = \mathbb{E}\{\zeta(\mathbf{x}_{\Gamma})\}/\sigma\{\zeta(\mathbf{x}_{\Gamma})\})$ is equal to 0.3.

2.5. Monte Carlo simulation parameters

For each set of perturbation parameters, we construct 1000 head models. These 1000 head models are used to determine the distribution of the Dice scores of the perturbation. BEM simulations are conducted on the ensemble of head models. Then, the statistical moments of the E-field induced mid-depth into the GM compartment on a 40 mm × 40 mm motor cortex region centered directly below the coil are computed from the ensemble E-field results. We additionally compute the average coefficient of variation (CV)defined as $CV = \overline{\sigma}/\overline{\mu}$, where $\overline{\sigma}$ denotes the average of standard deviation in the domain and $\overline{\mu}$ denotes the average of the mean values in the domain.

3. Results

3.1. Individual tissue boundary shape uncertainty

First, the uncertainty in the E-field distribution introduced individually by each tissue boundary is investigated. Here only results for the Ernie head model are included [22], two additional head models with the same uncertain parameters where also considered in this study and similar findings where found (the additional results are included in the supplementary material available online at stacks.iop.org/JNE/19/026022/mmedia). Five tissue boundaries are considered in this work, i.e. air/scalp, scalp/skull, skull/CSF, CSF/GM, and GM/WM, as seen in figure 3(A). To determine the perturbation parameters on each tissue boundary, the Dice scores for the five corresponding tissue types, i.e. scalp, skull, CSF, GM, and WM are carefully calibrated with the reference result in [20] (See the upper panel green boxes in figure 3 therein). The perturbation parameters are given in table 1 and the corresponding Dice scores are shown in figure 3(B). The mean values of the Dice scores of this work is consistent

with the reference results. The variation of Dice scores originated from the random field of perturbations, while in [20] the variation originates from the intrinsic probabilistic segmentation process. In other words, the tissue boundary uncertainty in our work is within the range of what is expected from segmentation algorithms. The cortical E-field distribution without any tissue boundary shape uncertainty is shown in figure 3(C). The mean and standard deviation of the E-field distribution resulting from uncertain tissue boundary shapes are shown in figure 3(D). The mean E-fields are similar across tissue types and they coincide with the nominal results. The air/scalp or scalp/skull boundary shape uncertainty results in near zero standard deviation everywhere, and a maximum standard deviation is 0.08 and 2.92 V m⁻¹, respectively. This indicates that the Efield results are largely insensitive to scalp compartment segmentation accuracy. Furthermore, GM/WM boundary shape uncertainty also results in low standard deviation E-field everywhere, and has a maximum of 1.28 V m⁻¹. In contrast, skull/CSF or CSF/GM boundary shape uncertainty leads to large standard deviation of the E-field and the maximum standard deviations are 22.8 and 25.01 V m⁻¹, respectively. All of these results indicate that improving the segmentation accuracy of the CSF compartment is critical for reducing uncertainty in TMS simulations. In the next section, we study the dependence of E-field uncertainty on CSF segmentation perturbation parameters, thereby, quantifying the relation between the CSF compartment segmentation fidelity and E-field uncertainty.

3.2. Parametric study of uncertainties of skull/CSF and CSF/GM boundary shapes

Here we study the dependence of standard deviation of E-fields on tissue boundary perturbation parameters for skull/CSF and CSF/GM boundaries individually. In particular, we consider the perturbation height and correlation length. Again, during each run we only perturb a single tissue boundary.

Figure 4 provides a visual guide of the smoothness of the skull/CSF and CSF/GM realizations as a function of correlation length. Specifically, it shows realizations of the normalized random field (i.e. by how much we perturb the surface at each point) for various correlation lengths. As the correlation length increases the realizations become more smooth. This can be seen by the increasing sizes of the blue/red regions with increasing correlation length. Correspondingly, by increasing the correlation length, we increase the smoothness of the perturbations. This gives a way to control the curvature of the realizations.

First we consider the skull/CSF boundary. The mean and standard deviation for a fixed correlation length of 1.0 cm and a perturbation height of 1.0, 2.0 and 3.0 mm of the skull/CSF boundary are shown in figure 5. With increasing perturbation

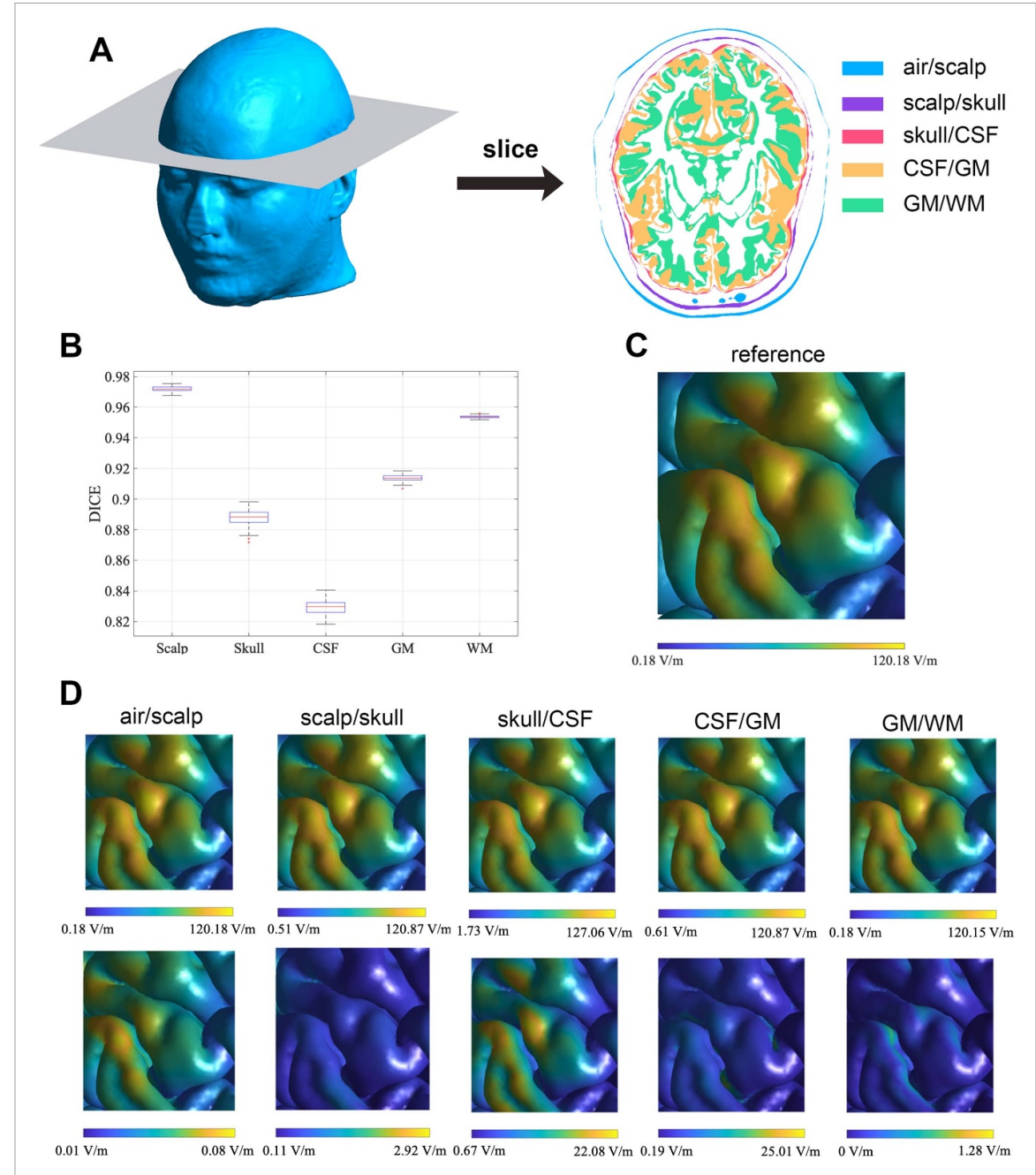


Figure 3. (A) Five brain boundaries are employed as the nominal surfaces, where the perturbations are generated. (B) Perturbation height on each tissue boundary is calibrated by calculation of Dice scores, which is comparable with the results using conventional segmentation algorithm in [20]. (C) The nominal E-field obtained from the head model without geometric uncertainties. (D) Contours of mean (first raw) and standard deviation (second raw) of E-fields with geometric perturbations on each single brain boundary.

Table 1. Perturbation parameters to compute Dice scores. The perturbation parameters are carefully chosen such that the corresponding Dice score of each tissue type is close to the results in [20].

	Air/Scalp	Scalp/Skull	Skull/CSF	CSF/GM	GM/WM
Perturbation height (mm)	1	2.5	2	1	1
Correlation length (mm)	20	20	10	5	5

height, the standard deviation increases significantly. Furthermore, the averaged coefficient of variation, which indicates the overall variation of the E-field, increases by a factor of 2.6 as the uncertainty height increases from 1.0 to 3.0 mm, as seen in figure 7(A). This indicates that significant reduction

in uncertainty can be achieved from a more accurate representation of the skull/CSF boundary. It can be also observed that the high standard deviations are all concentrated in the gyral crown regions. In addition to the perturbation height, we further consider the effects of correlation length on E-field

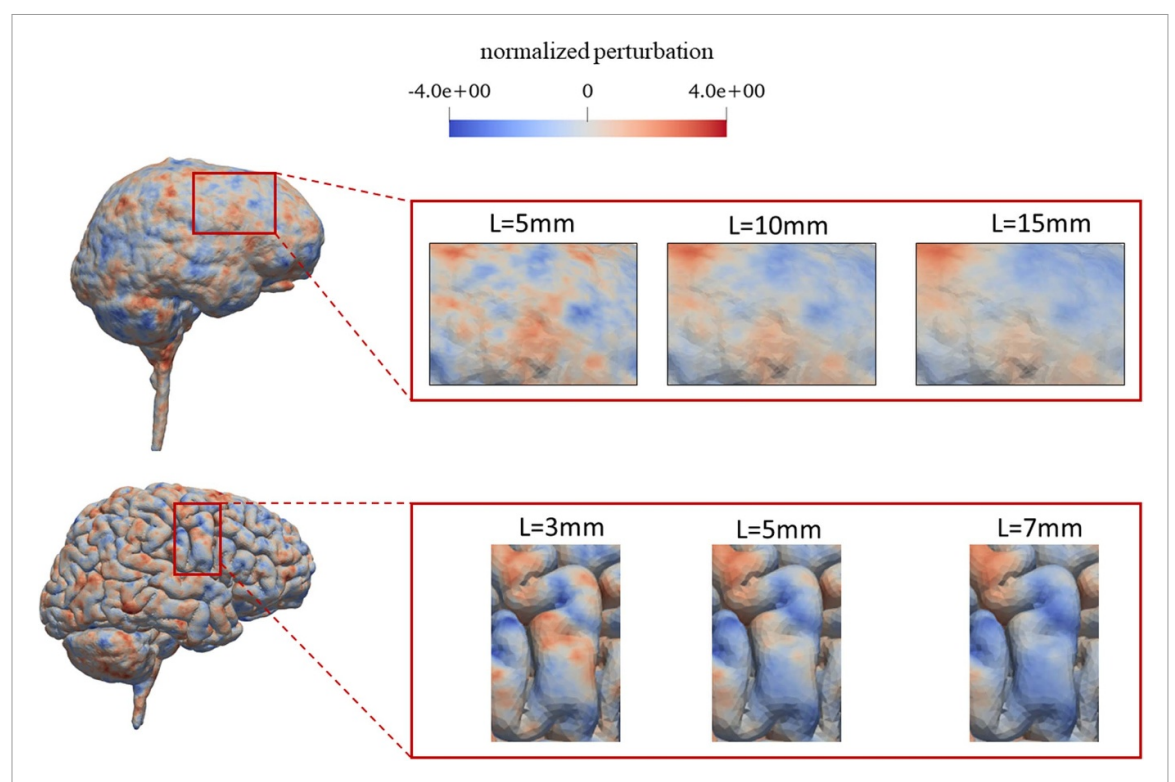


Figure 4. Realization of the normalized random fields generated on the skull/CSF (upper panel) and CSF/GM (lower panel) with various correlation lengths. The correlation lengths for skull/CSF (upper panel) are 5, 10 and 15 mm and the correlation lengths for CSF/GM (lower panel) are 3, 5, and 7 mm. It can be seen that the larger the correlation length, the more homogeneous the random field.

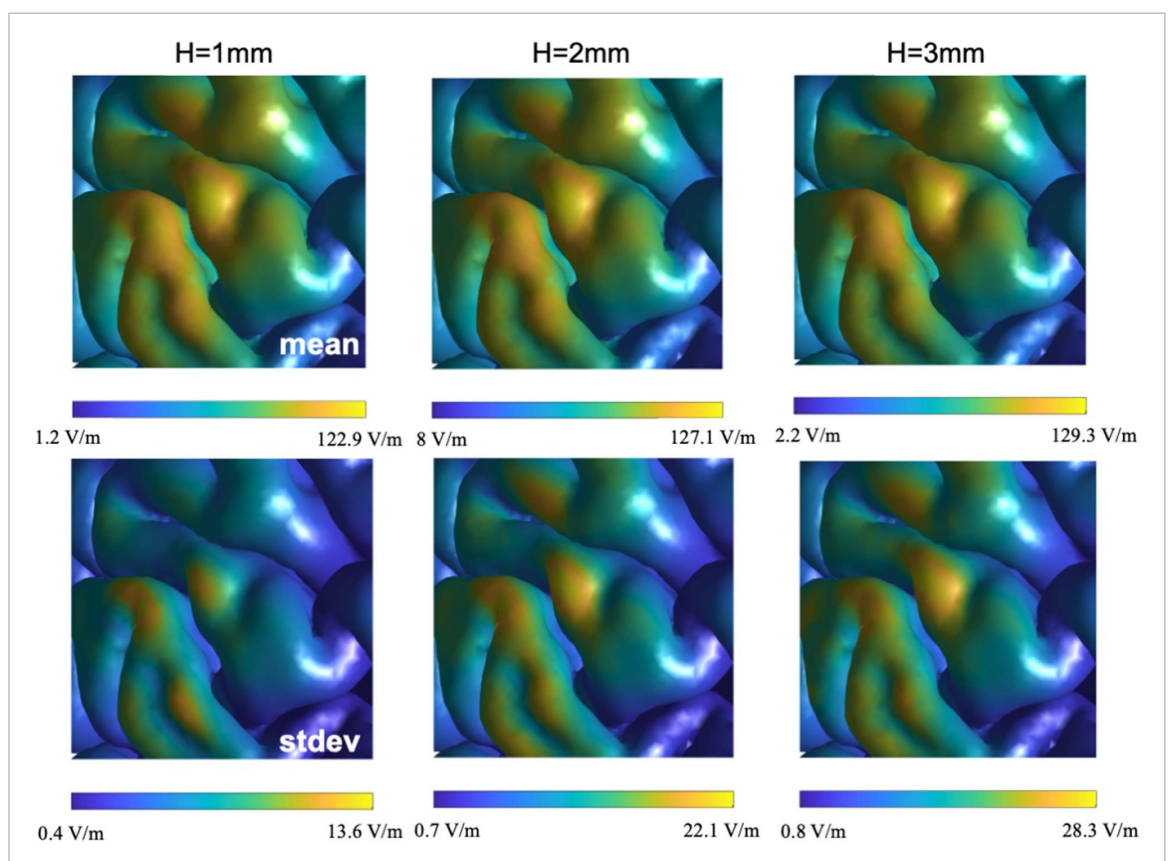


Figure 5. Contours of mean (first raw) and standard deviation (second raw) of E-fields with geometric uncertainties on skull/CSF boundary. Three perturbation heights are set for the random field, i.e. 1, 2 and 3 mm respectively, and correlation lengths are set as 1.0 cm for all. Left and right labels in color bar denote the minimum and maximum values in the corresponding contour.

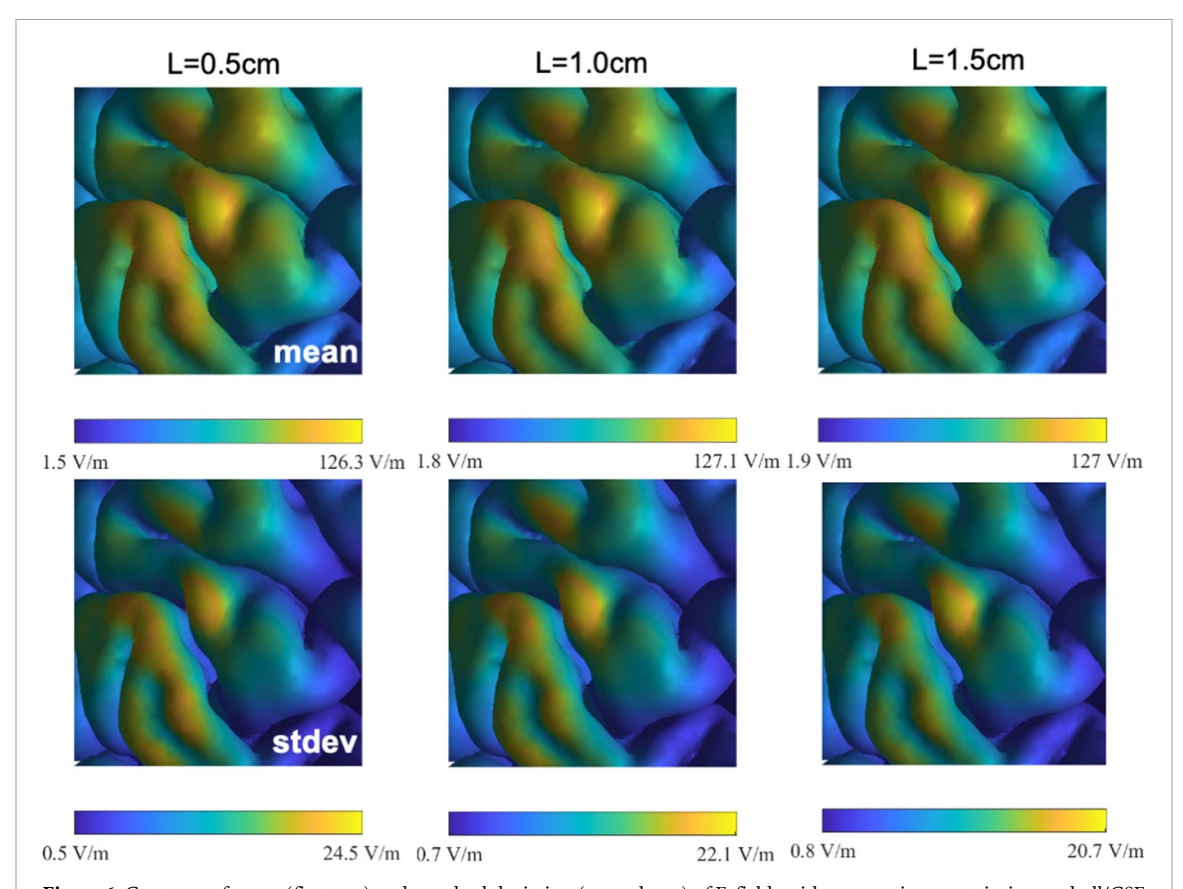


Figure 6. Contours of mean (first raw) and standard deviation (second raw) of E-fields with geometric uncertainties on skull/CSF boundary. Three correlation lengths are set for the random field, i.e. 0.5, 1.0 and 1.5 cm respectively, and perturbation heights are set as 2 mm for all. Left and right labels in color bar denote the minimum and maximum values in the corresponding contour.

uncertainty. The standard deviation of the E-field is calculated under correlation length of 0.5, 1.0 and 1.5 cm, respectively, while the perturbation height is fixed as 2.0 mm. The random field is in the upper panel of figure 4. The corresponding E-fields are shown in figure 6. As the correlation length increases both of the ranges of mean and standard deviation remain unaffected. Furthermore, the averaged coefficient of variation remains almost constant with the increasing correlation lengths from 0.5 to 1.5 cm, as shown in figure 7(B). This indicates that only a rough estimate of the correlation length of the segmentation uncertainty on skull/CSF is necessary to achieve satisfactory E-field uncertainty estimates.

Second we consider the CSF/GM boundary. The mean and standard deviation for a fixed correlation length of 5 mm and a perturbation height of 0.25, 0.5, and 0.75 mm of the CSF/GM boundary are shown in figure 8. Again, with increasing perturbation height, the standard deviation increases significantly. In contrast to the sulci, where the standard deviation is large, the gyral crown exhibits relatively low uncertainty. In other words, E-field predictions on the gyral crown are more robust to errors in the shape of CSF/GM boundary. The averaged coefficient of variation again increases nearly linearly with increasing uncertainty and it increases by a factor of 3 with

increasing perturbation height from 0.25 to 0.75, as seen in figure 10(A). Finally, we consider the effects of correlation length. The lower panel of figure 4 shows the random fields with correlation lengths of 3, 5, and 7 mm, respectively. The corresponding E-fields are shown in figure 9 with perturbation heights of 0.5 mm. The three sets of results are nearly identical. Furthermore, the averaged coefficient of variation is unchanged as the correlation length varies from 3 to 7 mm, as shown in figure 10(B). These results indicate that only a rough estimate of the correlation length of the segmentation uncertainty on CSF/GM boundary is necessary to compute satisfactory estimates of E-field uncertainty.

3.3. CSF compartment shape uncertainty

Here we consider the *combined* effects of shape uncertainties on skull/CSF and CSF/GM boundaries on TMS simulation results. Results for single skull/CSF, CSF/GM and their combined boundary uncertainty are shown in figure 11. With increasing correlation length the standard deviation of the E-field increases. Furthermore, the standard deviation of the combined effects is well approximated by assuming each of the skull/CSF and CSF/GM boundaries independently affect the E-field predictions. The skull/CSF and CSF/GM mostly introduce uncertainty in E-field predictions on the gyral crowns, and sulci, respectively.

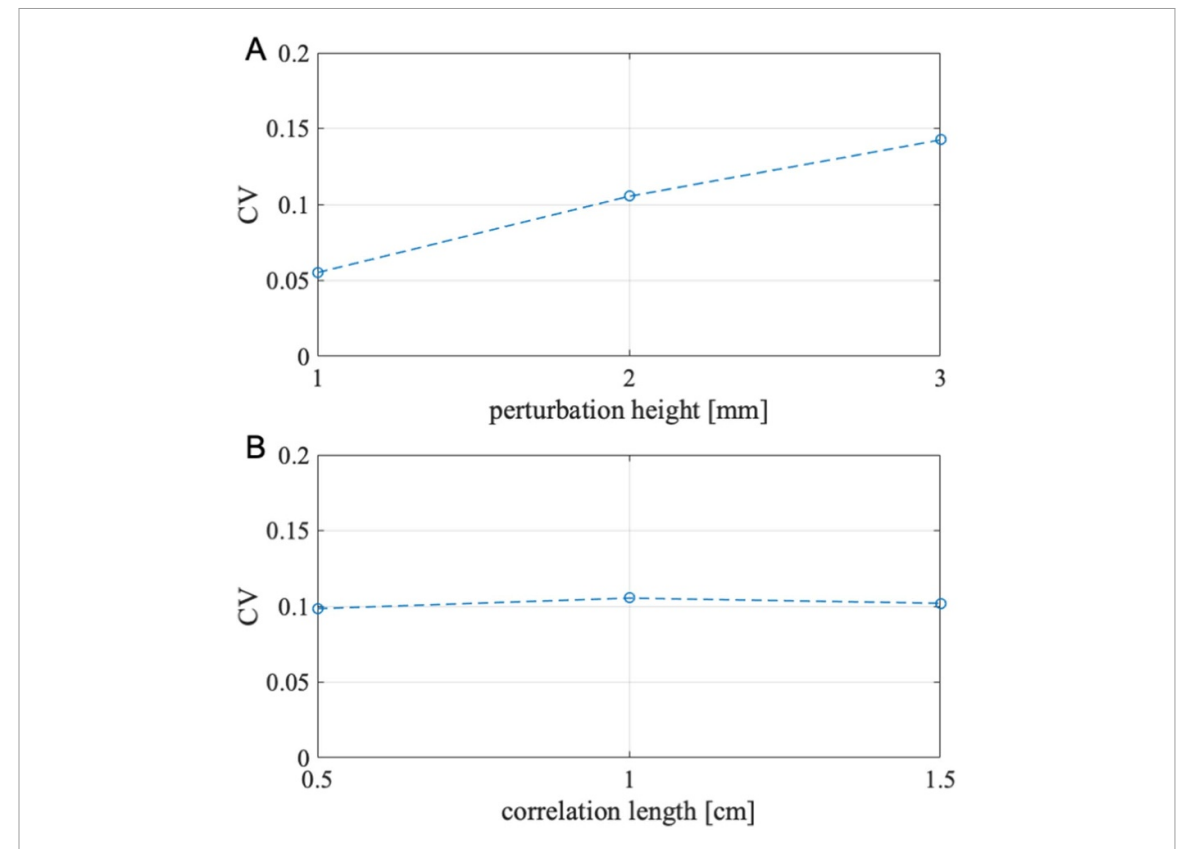


Figure 7. Coefficients of variation (CV) of E-fields with various perturbation heights and correlation lengths. Geometric uncertainties are only generated on skull/CSF boundary.

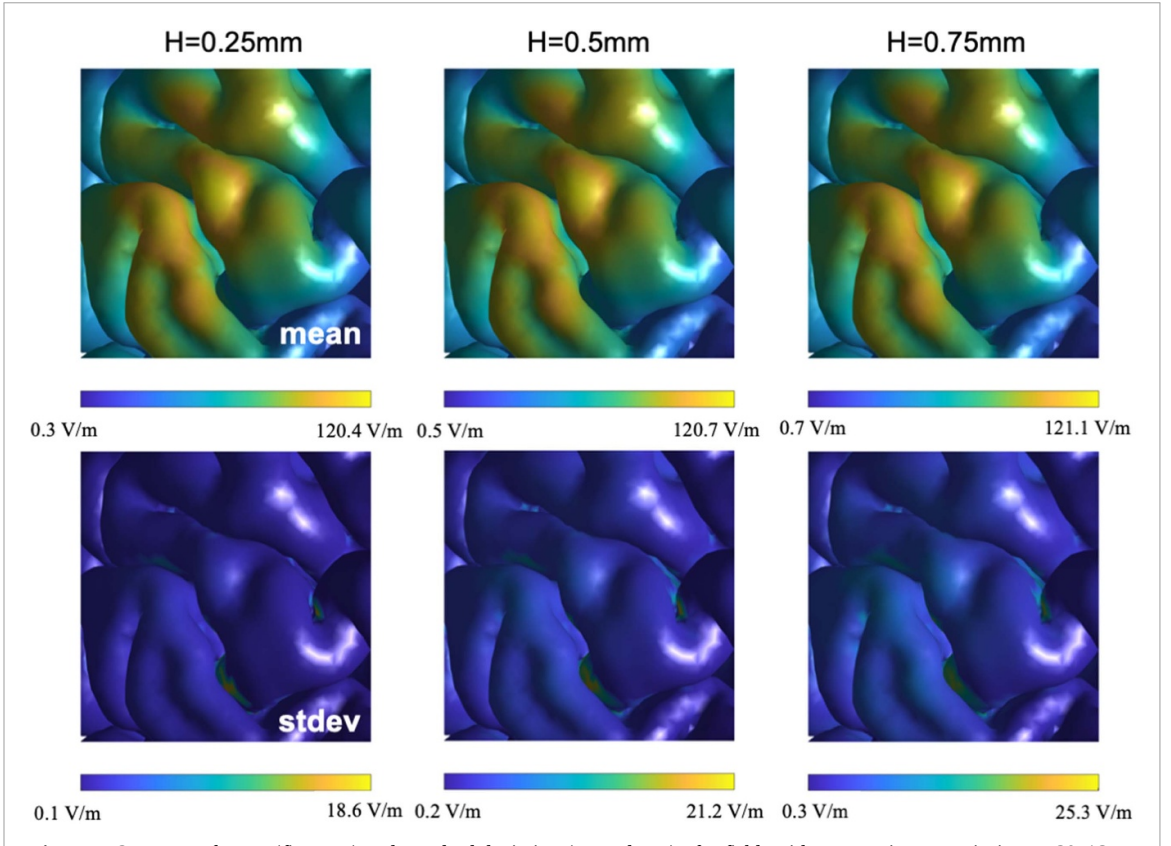


Figure 8. Contours of mean (first raw) and standard deviation (second raw) of E-fields with geometric uncertainties on CSF/GM boundary. Three perturbation heights are set for the random field, i.e. 0.25, 0.5 and 0.75 mm respectively, and correlation lengths are set as 5 mm for all. Left and right labels in color bar denote the minimum and maximum values in the corresponding contour.

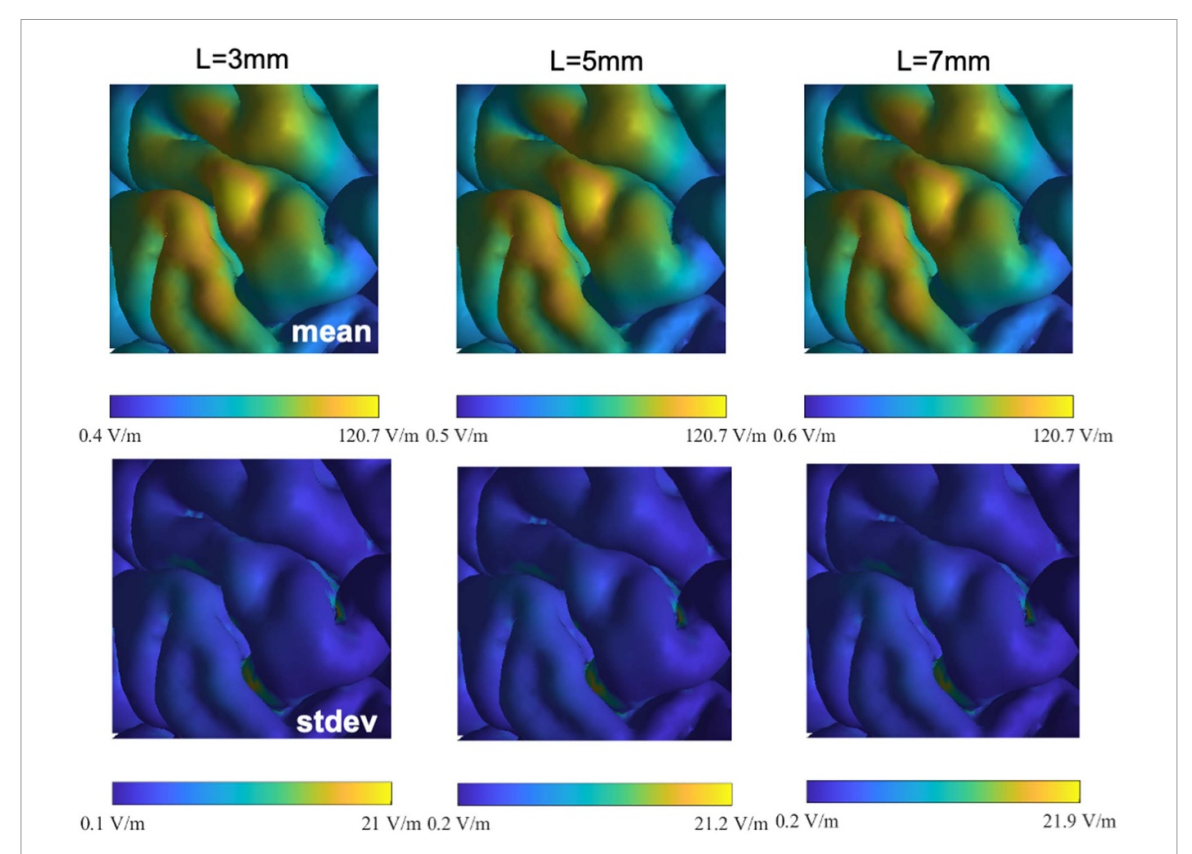
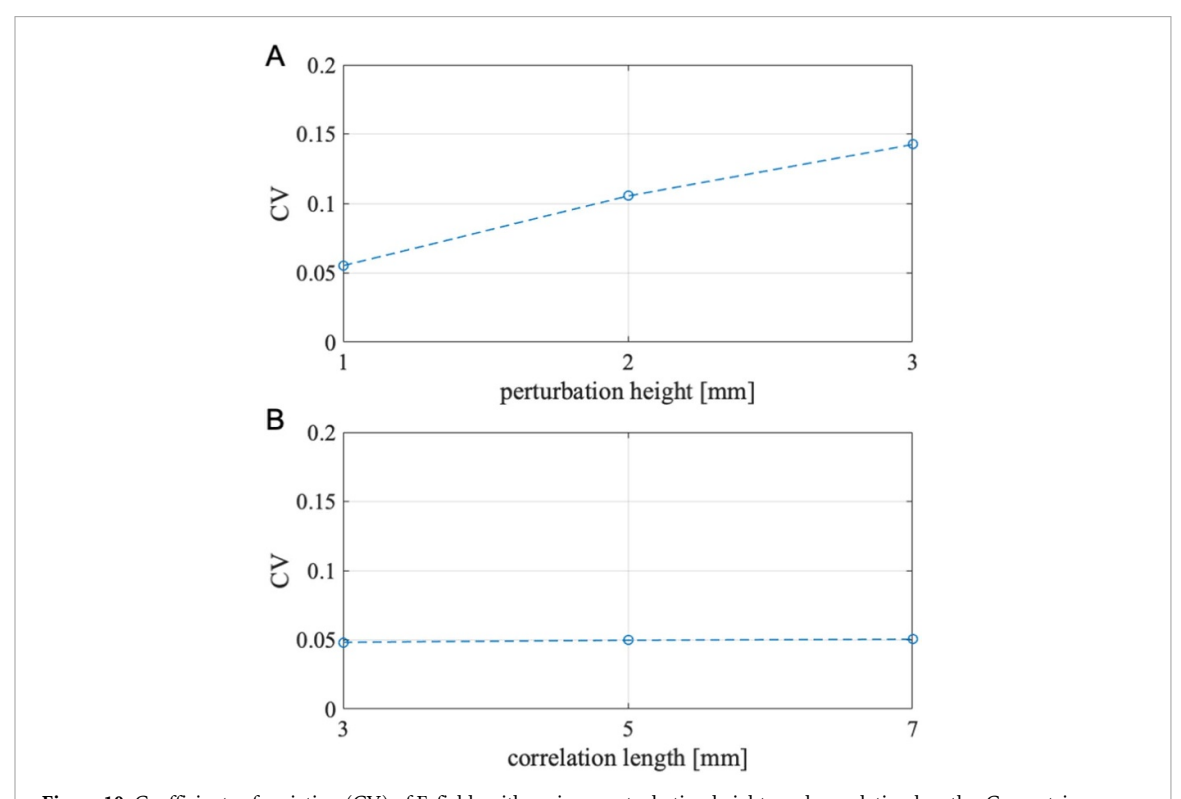


Figure 9. Contours of mean (first raw) and standard deviation (second raw) of E-fields with geometric uncertainties on skull/CSF boundary. Three correlation lengths are set for the random field, i.e. 3, 5 and 7 cm respectively, and perturbation heights are set as 0.5 mm for all. Left and right labels in color bar denote the minimum and maximum values in the corresponding contour.



 $\textbf{Figure 10.} \ \ Coefficients \ of \ variation \ (CV) \ of \ E-fields \ with \ various \ perturbation \ heights \ and \ correlation \ lengths. \ Geometric \ uncertainties are only generated on skull/CSF boundary.$

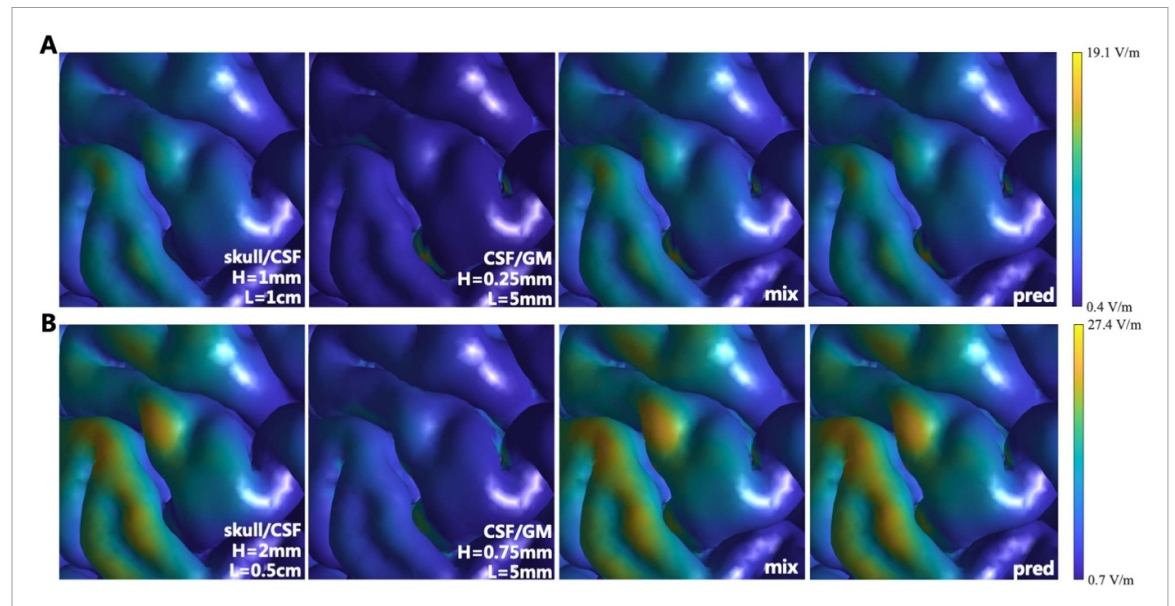


Figure 11. Contours of standard deviation of E-fields for set 1 (first raw) and set 4 (second raw) in figure 12. First column denotes the E-field standard deviation contour only using perturbed skull/CSF boundary, second column denotes the E-field standard deviation contour only using perturbed CSF/GM boundary, and third column denotes the E-field standard deviation contour using both perturbed skull/CSF and CSF/GM boundaries. The last column denotes the predicted E-field standard deviation contour calculated from the first and second contours as shown in equation (12).

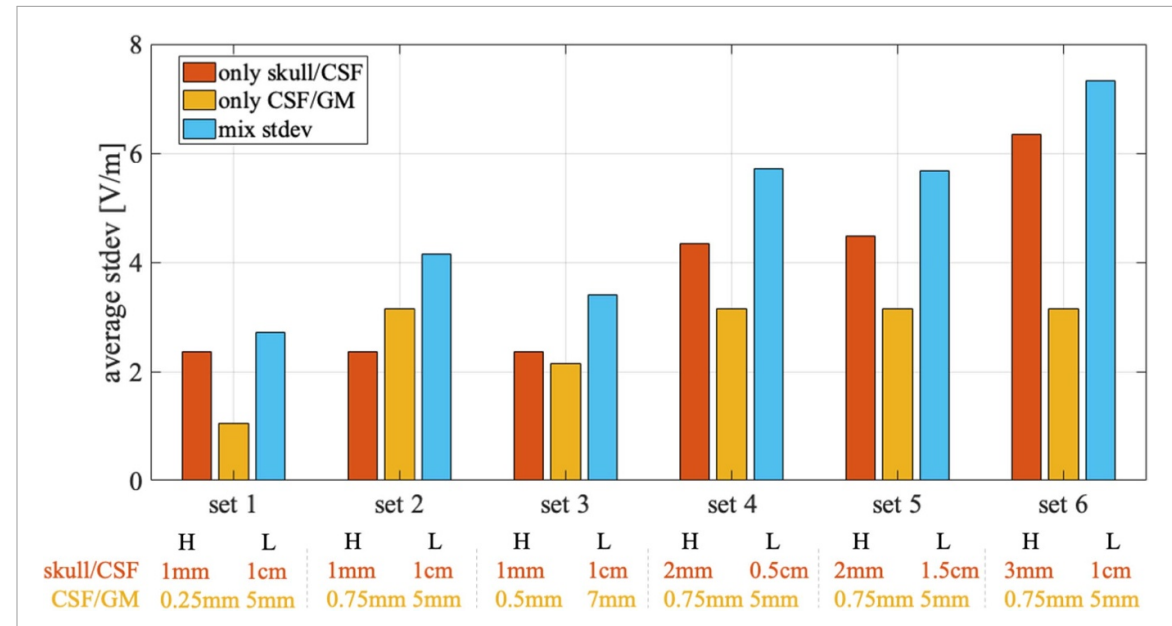


Figure 12. Averaged standard deviation of E-fields with geometric uncertainties on two single boundaries separately and their combined effect. Each set consists of the averaged standard deviation of E-field with geometric uncertainties only on skull/CSF boundary (red) and CSF/GM boundary (yellow), and geometric uncertainties on both boundaries (blue). Six sets are shown with various perturbation heights (H) and correlation lengths (L).

In other words, the effects of each tissue boundary on E-field are spatially separated, which partially could explain why their effects appear to be independent. Furthermore, the standard deviation is higher when both boundary shapes are perturbed compared with only one boundary perturbed.

We ran four additional scenarios and the results are consistent with the two presented in figure 11. Summary results for the six sets of mixed effect simulations are shown in figure 12. For all sets, the standard deviation of the E-field in the mixed effects cases

are well approximated as the square root of the square sum of the individual tissue standard deviation. In other words, the standard deviation can be approximated as:

$$\sigma_{pred} = \sqrt{(\sigma_1^2 + \sigma_2^2)},\tag{12}$$

where σ_{pred} is the predicted standard deviation of each node with two perturbed boundaries, σ_1 and σ_2 denote the standard deviations with only single skull/CSF or CSF/GM boundary respectively. The

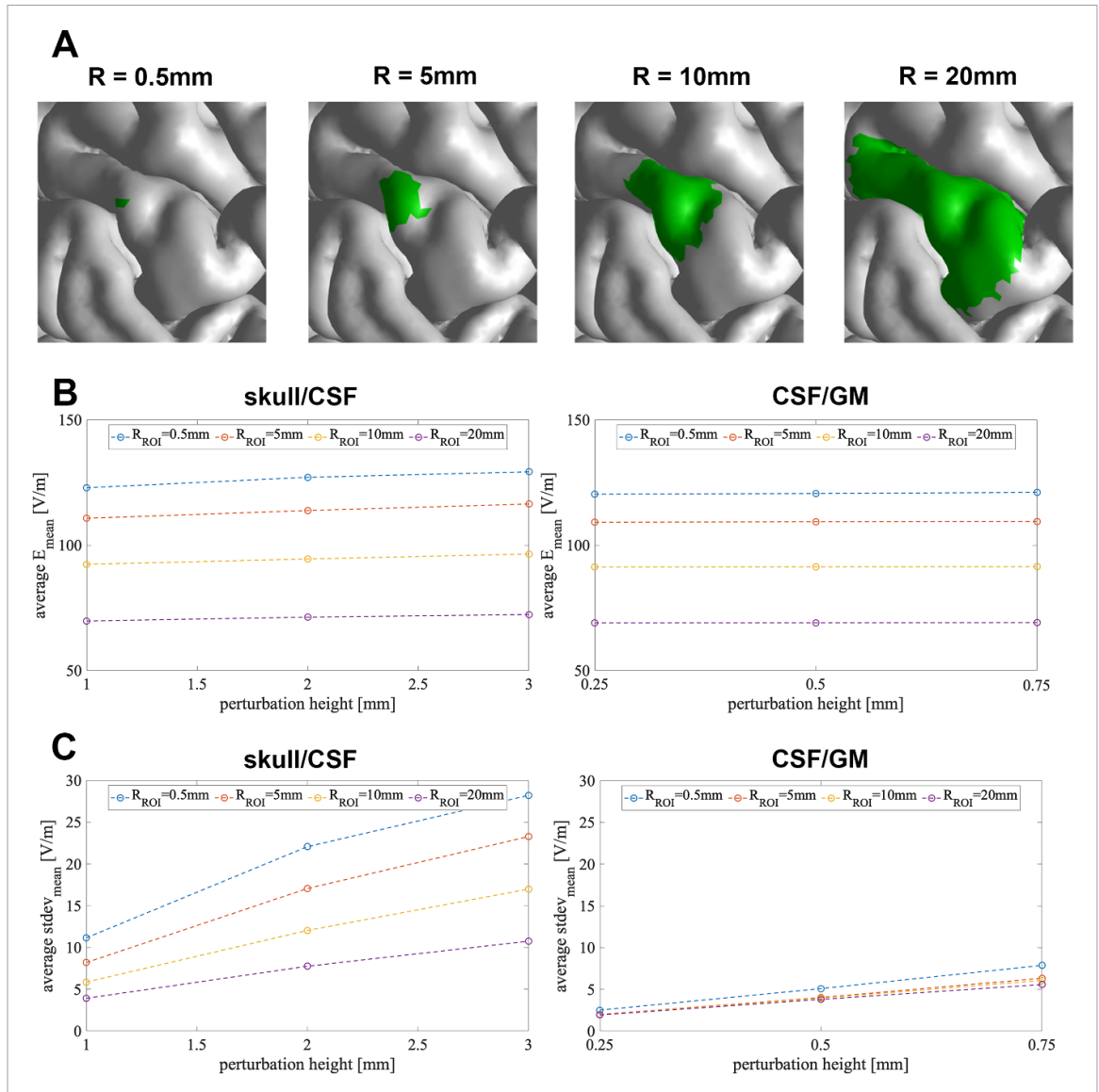


Figure 13. (A) The quantities of interest, i.e. the averaged mean and standard deviation of E-fields, are calculated in the ROI with various sizes. (B) The averaged mean of E-fields in ROI with perturbations generated on skull/CSF and CSF/GM boundaries separately, and (C) the averaged standard deviation of E-fields in ROI with perturbations generated on skull/CSF and CSF/GM boundaries separately.

observed differences of E-field standard deviation between the calculated and predicted results using the above equation ranged between 0.45% and 2.0% for the six sets. This gives a fast way to approximate standard deviations from combined effects using single boundary shape uncertainty results.

3.4. Robustness of mean E-field

The above sections, we have considered the pointwise uncertainty of the E-field distribution on a cortical region. However, oftentimes the E-field is averaged over a region of interest (ROI) to define the total E-field dose delivered to it. This section studies the uncertainty introduced in the the averaged E-field over an ROI as a function of ROI size and perturbation parameters. Note that only the perturbation height is considered here, since the E-fields are almost stable with the correlation lengths as shown in the

above sections. Specifically, we consider ROIs shown in figure 13(A), with radii of 0.5, 5, 10 and 20 mm, respectively. The averaged mean and standard deviation on the E-fields in each ROI as a function of varying perturbation heights is shown in figures 13(B) and (C), left column showing the perturbation on skull/CSF boundary, and right column showing the perturbation on CSF/GM boundary. The averaged mean E-fields in ROI are stable regardless of the ROI size or the perturbation height. Furthermore, the larger is the ROI size, the smaller is the overall variation in the E-field in the targeted ROI; this is particularly more visible for the skull/CSF boundary. For example, assuming a skull/CSF boundary with perturbation height of 2 mm, ROIs of radii of 0.5, 5, 10 and 20 mm have standard deviations of 22.07, 17.06, 12.04, 7.76 V m^{-1} , respectively. Both of the observations have indicated that the averaged E-field over

a region is more robust to segmentation errors than pointwise E-field estimates.

4. Discussion

During TMS the skull acts like an insulator that limits the amount of conduction current flowing between the skin and intracranial regions. This is consistent with the low sensitivity of the cortical E-fields to air/scalp and scalp/skull boundary uncertainty. The skull/CSF boundary is a transition between a low-conductivity region to a large one. Correspondingly, conduction currents in the CSF compartment are mostly tangential to the skull/CSF boundary. The gyral crowns are closer to the skull/CSF boundary than the sulci. The near proximity of skull/CSF boundary could explain the large sensitivity of E-fields on gyral crown regions to skull/CSF perturbations. The skull/CSF boundary is nearly tangential to the gyral crowns. As a result, there is little charge buildup on the gyral crowns of the CSF/GM boundary. This could explain why we observe little uncertainty in E-field predictions on the gyral crown resulting from uncertainty in CSF/GM boundary shape. In contrast, the sulci are nearly perpendicular to the skull/CSF boundary, and by proxy CSF compartment E-fields. Correspondingly, there is a large charge build-up on CSF/GM boundary regions of the sulci. This charge build-up could explain the relatively large sensitivity of E-fields on sulci regions to CSF/GM boundary shape. Note that another study [25] considered E-field dependence on sulci width (i.e. shape) and found similar results. Specifically, it was found that sulci width (i.e. variations of CSF/GM surface) results in variations in sulci predicted E-field while the E-fields on the crown are largely unaffected.

Uncertainty quantification results have shown that within realistic ranges, the predictions are robust to changes in correlation length. This means that although we do not have a precise description of the correlation structure of the uncertainty, the results are likely still valid. For the cases studied here, it is also observed that the standard deviation of the E-field generated by perturbing both of the skull/CSF and CSF/GM interfaces can be well approximated from the single boundary perturbation results; this is likely because of the fact that the two boundaries largely introduce E-field uncertainty in spatially distinct regions.

For standardization of the E-field dose, and quantitative studies of dose and response, it is important to be able to compute an E-field related quantity that is robust to uncertainty in the TMS setup. Preliminary results indicate that the average E-field on a cortical ROI is more robust to uncertainty than pointwise estimates of the E-field. A detailed study of generalizability of these results to other brain regions and head models is beyond the scope of this paper and could be the subject of a future study. Furthermore, other

common ROI E-field parameters like the 99 percentile E-field could have even lower uncertainties, but we did not consider these here.

5. Conclusion

For TMS computational E-field dosimetry there are a number of factors contributing to uncertainty in E-field predictions. This manuscript studied the uncertainty of cortical E-field predictions introduced by segmentation uncertainty in the head model geometry. Our results showed that uncertainty in the shape of the skull/CSF and CSF/GM boundaries results in significant uncertainty in the E-field predictions. Furthermore, air/scalp, scalp/skull, and GM/WM boundaries resulted in negligible uncertainty. Finally, averaging the E-field over a small region resulted in smaller uncertainty than was observed for point-wise estimates of the E-field.

Data availability statement

All data that support the findings of this study are included within the article (and any supplementary files). This paper develops the first methodology for studying how possible errors in the segmentation of MRI images can impact the E-field predictions of Transcranial Magnetic Stimulation simulations.

Acknowledgments

Research reported in this publication was supported by the National Institute of Mental Health of the National Institutes of Health under Award Number R00MH120046. The content of current research is solely the responsibility of the authors and does not necessarily represent the official views of the National Institutes of Health. The work of the J. G. was partially supported by the National Science Foundation, USA, Division of Civil, Mechanical and Manufacturing Innovation, under award CMMI-1942928.

ORCID iD

Luis J Gomez https://orcid.org/0000-0002-7699-2160

References

- [1] Ellison A and Cowey A 2007 Time course of the involvement of the ventral and dorsal visual processing streams in a visuospatial task *Neuropsychologia* 45 3335–9
- [2] Levit-Binnun N, Handzy N Z, Moses E, Modai I and Peled A 2007 Transcranial agnetic stimulation at m1 disrupts cognitive networks in schizophrenia Schizophrenia Res. 93 334–44
- [3] Pascual-Leone A, Walsh V and Rothwell J 2000 Transcranial magnetic stimulation in cognitive neuroscience—virtual lesion, chronometry, and functional connectivity Curr. Opin. Neurobiol. 10 232–7

- [4] Pitcher D, Walsh V, Yovel G and Duchaine B 2007 TMS evidence for the involvement of the right occipital face area in early face processing *Curr. Biol.* 17 1568–73
- [5] Rothwell J C 1999 Paired-pulse investigations of short-latency intracortical facilitation using TMS in humans Electroencephalogr. Clin. Neurophysiol. 51 113–9
- [6] Rossini P M and Rossi S 2007 Transcranial magnetic stimulation—diagnostic, therapeutic and research potential Neurology 68 484–8
- [7] Wassermann E M and Zimmermann T 2012 Transcranial magnetic brain stimulation: therapeutic promises and scientific gaps *Pharm. Ther.* 133 98–107
- [8] O'Reardon J P et al 2007 Efficacy and safety of transcranial magnetic stimulation in the acute treatment of major depression: a multisite randomized controlled trial Biol. Psychiatry 62 1208–16
- [9] Lipton R B, Dodick D W, Silberstein S D, Saper J R, Aurora S K, Pearlman S H, Fischell R E, Ruppel P L and Goadsby P J 2010 Single-pulse transcranial magnetic stimulation for acute treatment of migraine with aura: a randomised, double-blind, parallel-group, sham-controlled trial *Lancet Neurol*. 9 373–80
- [10] Peterchev A V, Wagner T A, Miranda P C, Nitsche M A, Paulus W, Lisanby S H, Pascual-Leone A and Bikson M 2012 Fundamentals of transcranial electric and magnetic stimulation dose: definition, selection and reporting practices *Brain Stimul.* 5 435–53
- [11] Gomez L J, Dannhauer M, Koponen L M and Peterchev A V 2020 Conditions for numerically accurate tms electric field simulation *Brain Stimul.* 13 157–66
- [12] Saturnino G B, Madsen K H and Thielscher A 2019 Electric field simulations for transcranial brain stimulation using FEM: an efficient implementation and error analysis *J. Neural Eng.* 16 066032
- [13] Thielscher A, Opitz A and Windhoff M 2011 Impact of the gyral geometry on the electric field induced by transcranial magnetic stimulation *Neuroimage* 54 234–43
- [14] Saturnino G B, Thielscher A, Madsen K H, Knösche T R and Weise K 2019 A principled approach to conductivity uncertainty analysis in electric field calculations *NeuroImage* 188 821–34
- [15] Gomez L J, Dannhauer M and Peterchev A V 2021 Fast computational optimization of TMS coil placement for individualized electric field targeting *NeuroImage* 228 117696
- [16] Bigoni D, Engsig-Karup A P and Marzouk Y M 2016 Spectral tensor-train decomposition SIAM J. Sci. Comput. 38 A2405–39
- [17] Wells W M, Grimson W E L, Kikinis R and Jolesz F A 1996 Adaptive segmentation of MRI data *IEEE Trans. Med. Imaging* 15 429–42
- [18] Zhang Y, Brady M and Smith S 2001 Segmentation of brain MR images through a hidden Markov random field model and the expectation-maximization algorithm *IEEE Trans. Med. Imaging* 20 45–57
- [19] Henschel L, Conjeti S, Estrada S, Diers K, Fischl B and Reuter M 2020 Fastsurfer—a fast and accurate deep learning based neuroimaging pipeline NeuroImage 219 117012
- [20] Puonti O, Van Leemput K, Saturnino G B, Siebner H R, Madsen K H and Thielscher A 2020 Accurate and robust whole-head segmentation from magnetic resonance images for individualized head modeling *NeuroImage* 219 117044
- [21] Cardinale F et al 2014 Validation of freesurfer-estimated brain cortical thickness: comparison with histologic measurements Neuroinformatics 12 535–42
- [22] Nielsen J D, Madsen K H, Puonti O, Siebner H R, Bauer C, Madsen C G, Saturnino G B and Thielscher A 2018

- Automatic skull segmentation from MR images for realistic volume conductor models of the head: assessment of the state-of-the-art *NeuroImage* 174 587–98
- [23] Huang Y, Datta A, Bikson M and Parra L C 2019 Realistic volumetric-approach to simulate transcranial electric stimulation-roast-a fully automated open-source pipeline J. Neural Eng. 16 056006
- [24] Mikkonen M and Laakso I 2019 Effects of posture on electric fields of non-invasive brain stimulation *Phys. Med. Biol.* 64 065019
- [25] Janssen A M, Rampersad S M, Lucka F, Lanfer B, Lew S, Aydin U, Wolters C H, Stegeman D F and Oostendorp T F 2013 The influence of sulcus width on simulated electric fields induced by transcranial magnetic stimulation *Phys. Med. Biol.* 58 4881–96
- [26] Rashed E A, Gomez-Tames J and Hirata A 2021 Influence of segmentation accuracy in structural MR head scans on electric field computation for TMS and TES *Phys. Med. Biol.* 66 064002
- [27] Adler R J 2010 The Geometry of Random Fields (Philadelphia, PA: SIAM)
- [28] Lindgren F, Rue H and Lindström J 2011 An explicit link between Gaussian fields and Gaussian Markov random fields: the stochastic partial differential equation approach *Proc. R. Soc.* B 73 423–98
- [29] Staber B and Guilleminot J 2017 Stochastic modeling and generation of random fields of elasticity tensors: a unified information-theoretic approach C. R. Mécanique 345 399–416
- [30] Staber B and Guilleminot J 2018 A random field model for anisotropic strain energy functions and its application for uncertainty quantification in vascular mechanics Comput. Methods Appl. Mech. Eng. 333 94–113
- [31] Melancon D, Bagheri Z, Johnston R, Liu L, Tanzer M and Pasini D 2017 Mechanical characterization of structurally porous biomaterials built via additive manufacturing: experiments, predictive models, and design maps for load-bearing bone replacement implants, *Acta Biomater*. 63 350–68.
- [32] Bansal R, Staib L H, Xu D, Zhu H and Peterson B S 2007 Statistical analyses of brain surfaces using Gaussian random fields on 2-d manifolds *IEEE Trans. Med. Imaging* 26 46–57
- [33] Zhang H, Guilleminot J and Gomez L J 2021 Stochastic modeling of geometrical uncertainties on complex domains, with application to additive manufacturing and brain interface geometries Comput. Methods Appl. Mech. Eng. 385 114014
- [34] Ashburner J and Friston K J 2005 Unified segmentation Neuroimage 26 839–51
- [35] Rashed E A and Hirata A 2020 CondNet: deep learning architecture for electrical conductivity estimation of human head models IEICE Tech. Rep. 119 13–17
- [36] Gomez L J, Sheng W, Yucel A C and Michielssen E 2019 Fast statistical characterization of rough surface scattering via tensor train decompositions CNC-USNC/URSI National Radio Sci. Meet
- [37] Whittle P 1954 On stationary processes in the plane Biometrika 41 434–49
- [38] Makarov S N, Noetscher G M, Raij T and Nummenmaa A 2018 A quasi-static boundary element approach with fast multipole acceleration for high-resolution bioelectromagnetic models *IEEE Trans. Biomed. Eng.* 65 2675–83
- [39] Gomez L 2019 TMS E-field solvers (available at: https://github.com/luisgo/TMS_Efield_Solvers)